Chapter 4

Synthesis, characterization, and hetero-photocatalytic studies of $Bi_4BaTi_4O_{15}$ ceramic

4.1 Introduction

Over the last few years, elevated worldwide attention is directed toward harvesting solar energy to remedy environmental pollutions and wastewater, which are the foremost threat to civilizations. Approximately 10-20 percent of dye synthesized in industries is lost during manufacturing and dyeing processes and thus, a considerate amount of non-fixed dye is released as wastewater by this industries (Naresh and Mandal 2014). Release of these colored textile effluents in the ecosystem is an explicit source of aesthetic pollution, eutrophication and cause of ample disruption in aquatic life, making it is a matter of serious concern as freshwater present on earth is only 0.5 % of total water present. Besides, every 20 years, the global consumption of water is doubling, which is surpassing twice the human population growth rate (Han et al. 2009). Thus, to ensure constant water supplies recycle, reuse and reclaiming of wastewater becomes quite crucial. Conventional anaerobic or chemical degradation of organic dyes readily yields carcinogenic products like aromatic amines, which are potentially hazardous and moreover, it creates more concentrated secondary pollutants that further alleviates the conundrum (Han et al. 2009).

Consequently, a better promising technology of chemical treatment of wastewaters based on oxidative degradation of organic dyes dispersed or dissolved in the aqueous medium is emerging as advanced oxidation process (AOP). Heterogeneous photocatalytic is of particular interest of such chemical-oxidative processes which are characterized by the generation of strongest oxidant known i.e. hydroxyl radicals and superoxide anion radicals, photogenerated by semiconductor photocatalyst in the presence of both water and atmospheric oxygen (Rana et al. 2005). The aromatic ring present in dyes undergoes successive attacks by radicals to finally evolve CO_2 and

H_2O, leading to complete mineralization of organic molecules into CO_2 and other simpler inorganic ions (Lachheb et al. 2002).

Key to the practical application of photocatalytic technology is to develop a photocatalysts that could efficiently utilize solar energy and prevent charge recombination effectively. Heterogeneous photocatalysis utilizing single-phase bulk and nanostructured metal oxides semiconductors sought interest in this regard (Naresh and Mandal 2014). The irradiated semiconductors generate holes and electrons, which may recombine before being employed in subsequent reactions. Thus, to sustain charge separation, strategies such as the formation of heterostructures, doping or enhancement of crystallinity are adopted (Li et al. 2017). Also, many other application in bio-related problems such as anti-microbial (Girase et al. 2011; Ma et al. 2015), elevation of biocompatibility (Ramos-Corella et al. 2019), disruption of biofilm (Depan and Misra 2014; Nune et al. 2017) has also been reported.

One category of materials exhibiting impressive high oxide ion conductivity and charge separation stable even around 900°C were bismuth layered pervoskites reported in 1949 by Aurivillius (Kendall et al. 1996). Aurivillius oxide semiconductors have recently evoked curiosity due to their unique electronic and complex layered crystal arrangement. Chemical formula of this Aurivillius phase of Bismuth Layered Perovskite ferroelectric materials is $(Bi_2O_2)^{2+}(A_{m-1}B_mO_{3m+1})^{2-}$ forming alternating layers , where A denotes large 12 co-ordinate cation (K^+, Na^+, Pb^{2+}, Ca^{2+}, Ba^{2+}, Sr^{2+}, Bi^{3+}) and rare earth elements, B represents small 6 co-ordinate cation (Ti^{4+}, Nb^{5+}, Ta^{5+}, Mo^{6+}, W^{6+}, etc.) and m=1- 5 indicates to the BO_6 octahedral number amidst adjacent $(Bi_2O_2)^{2+}$ layers(Liu et al. 2014). Besides, this peculiar crystalline structure governs the growth pattern in these materials. Polarization is thus

viable in two possible directions along the c-axis and a-axis, generating anisotropy as vectors keep switching the directions and by virtue of this behavior, these materials possess a high dielectric constant (Galasso and Kestigan 2007). The growth is also anisotropic, as platelets favoring the grain alignment parallel to the c-axis that permits crystal orientation and texture (Moure 2018). This layered structure, apart from providing better charge separation also shows enhanced feasibility for the separation as well as diffusion of electrons-holes pairs created by photons in comparison to the bulk non-layered photocatalysts (Liu et al. 2014). Pure titania as a semiconductor photocatalyst is characterized by low quantum efficiency and high rate of e and h+ recombination (Rana et al. 2006; Sunkara and Misra 2008; Venkatasubramanian et al. 2008). Separation is favorable as the lattice sites of oxidation and reduction are located in a secluded fashion on the edges and surface of the sheets of the ultrathin units. The photogenerated hole in layered crystalline structures just diffuses through the sub-nanometer length to reach the surface of sheets where interlayer water molecules trap them allowing the electron to freely and efficiently reach the sheets edges, thus enhancing charge separation (Liu et al. 2010). It has been also known now that presence of metal act as reservoir for photogenerated electrons (Misra et al. 2012; Liang et al. 2017). These features make them highly efficient photocatalyst. Moreover, many efficient photocatalyst is observed to be having Bi^{3+} as its one component. Bismuth plays an crucial as valence shell s orbital of Bi (6s) hybridize with valence shell p orbital of O (2p) to form hybridized valence band (VB) of relatively lesser energy and facilitates higher mobility of photogenerated holes, accelerating the oxidation reaction responsible for elevated photocatalytic efficiency aurivillius oxides which belong to the bismuth-layered perovskite ferroelectric materials family (Zhang et al. 2011 May). Aurivillius family not only sought great attention in recent years due to their photocatalytic activity but also in regards to the high range of dielectric

constant and low loss, and good fatigue endurance. Also, the occurrence of Bi^{3+} lone pairs on the A site of Aurivillius structure aids the distortion of perovskite instigates ferroelectricity in the materials and it has been witnessed that A-site cations are more effective in controlling the dielectric properties than BO_6 octahedra owing to the smaller size of B-site cations (Benedek et al. 2015). Few other mentionable potentials are their applications in various devices like random access memory (RAM), transducer, actuators, oxygen ion conductors, multiferroics, lead-free relaxor photoluminescent films and as already discussed it is an efficient photocatalyst for water purification and hydrogen production as well (Moure 2018).

Barium Titanate $Bi_4Ti_3O_{12}$ is one best-known typical compounds of Aurivillius oxides owing to its credible application in ferroelectric memories and optical devices and it has been intensively studied as a photocatalyst for water splitting and for degradation of organic pollutants. Regrettably, the conductivity of $Bi_4Ti_3O_{12}$ hinders the polarization and low photocatalytic efficiency of individual phase $Bi_4Ti_3O_{12}$ nanomaterials is obtained due to the rapid recombination of photoexcited electron-hole pairs (Liu et al. 2014). Thus, to improve the polling processes by structural modification, various other pervoskites have been added. $BaTiO_3$, one such pervoskite with colossal polarization spawning excellent ferroelectric and dielectric properties, is opted to add in $Bi_4Ti_3O_{12}$ to yield a new ceramic material $Bi_4BaTi_4O_{15}$ (BBTO) in the present work (Maradudin). BBTO belongs to the Aurivillius family where m = 4, which suggests it is even layered and thus, polarization only exists in the a-b-axis and missing along the c-axis. A-site in the perovskite is occupied by Ba and Bi ion while B-site by Ti ion (Nayak et al. 2015). Due to its peculiar crystal structure, BBTO exhibits anisotropic ferroelectricity and novel

electrical properties and with increased light harvesting, the prolonged lifetime of carriers enhanced catalytic performance as well as higher chemical stability.

4.2 Experimental Section

For chemical route synthesis of $Bi_4BaTi_4O_{15}$, starting materials taken were barium nitrate $Ba(NO_3)_2$ (99% Merck, India), $Bi(NO_3)_3.5H_2O$ (99% Merck, India), Titanium oxide (oxide TiO2 99% Merck, India) and citric acid (Citric acid $C_6H_8O_7$,99.5%, Emparta, India). The stoichiometric amount of Ba^{+2}, Bi^{+3}, Ti^{4+} and ions were dissolved in distilled water and citric acid, equivalent to metal ions was also added to this reaction mixture. The obtained reaction mixture was heated on a hot plate with continuous stirring at 70–80 °C to evaporate water. After removing water, a fluffy mass was obtained, which burnt with sooty flame at a higher temperature. The resulting ash was crushed with the help of agate and mortar to make a fine powder. The powder was calcined at 950 °C. Calcined powder was used to make cylindrical pellets with the help of a PVA binder on applying 5 tons of pressure for 60 seconds. The pellet was sintered at 950 °C for 8 h and further used for characterization and measurements.

4.2.1 Photocatalytic Experiment

Evaluation of the photocatalytic activity of the synthesized sample (BBTO) was done by analyzing the aerobic degradation of RhB in solar light. To execute the photocatalytic test, 0.6 mg photocatalyst and 3 ml aqueous solution of RhB (dye concentration 8.38 mg/L) were mixed in a quartz cuvette measuring path length of 1cm. To achieve the adsorption equilibrium prior to solar light irradiation, the reaction solution was stirred in the dark for 60 min and then the sample solution was exposed to solar light. The extent of degradation after specific time intervals was measured by recording the UV-Vis absorption spectra at wavelength 554 nm specific for RhB.

With the interest of identifying the active species responsible for the photocatalytic activity, 0.5 mM of isopropyl alcohol (IPA), parabenzoquinone (PBQ), and potassium iodide (KI) were added as scavengers for superoxide radicals ($O^{2\bullet-}$), hydroxyl radicals ($^{\bullet}OH$), and holes (h^{+}) in reaction mixture, respectively.

4.3 Characterization

The diffraction pattern of sintered $Bi_4BaTi_4O_{15}$ (BBTO) ceramic was recorded by X-ray diffractometer (XRD, Rigaku miniflex 600, Japan) using Cu-Kα radiation (λ = 1.54 Å) with 2°/min scan rate. The FTIR spectra were characterized using KBr pellets by ATR FTIR (Bruker, ALPHA model) Spectrophotometer in the frequency range 500–1500 cm^{-1}. UV-visible (UV-Vis) spectrum of sintered powder was examined by a UV-Vis spectrophotometer (UV2600, Shimadzu). The surface morphology of ceramic pellet was observed by scanning electron microscope (ZEISS model, EVO18 Germany) whereas its elemental compositions were analyzed by Energy dispersive X-ray (EDX) spectroscopy (Oxford instrument; USA). For determination of particle shape and size Transmission electron microscope (TEM, FEI TECANI G2 20 TWIN; USA) was employed. The zeta potential of the material was measured by a dynamic light scattering technique using a Zetasizer Nano-ZS (Malvern Instruments, Malvern, UK). The Brunauer–Emmett–Teller (BET) surface area was examined by nitrogen adsorption-desorption isotherm measurements at 77.350K on a Quantachrome NOVA2000E device. The pore size distribution plot was attained by the Barret–Joyner–Halenda (BJH) model. X-ray photoelectron spectra (XPS) was recorded using PHI 5000 Versaprobe II photoelectron spectrometer (ULVAC-PHI) using Al Kα X-ray beam. Magnetic measurements were accomplished with a Quantum Design MPMS-3, at applied a magnetic field of ±2 T over a temperature range 5–300 K.

Additionally, temperature dependent field cooling (FC) and Zero field cooling (ZFC) magnetization were recorded at 100 Oe applied field using SQUID VSM dc magnetometer at the same range of temperature.

4.4 Results and Discussion

Figure 4.1 displays high-resolution x-ray diffraction (HR-XRD) patterns of BBTO ceramic sintered at 950 °C for 8 h. The figures confirmed the single-phase formation of pure BBTO ceramic. All the diffraction patterns of HR-XRD spectra matched correctly with JCPDS card no (35-0757).

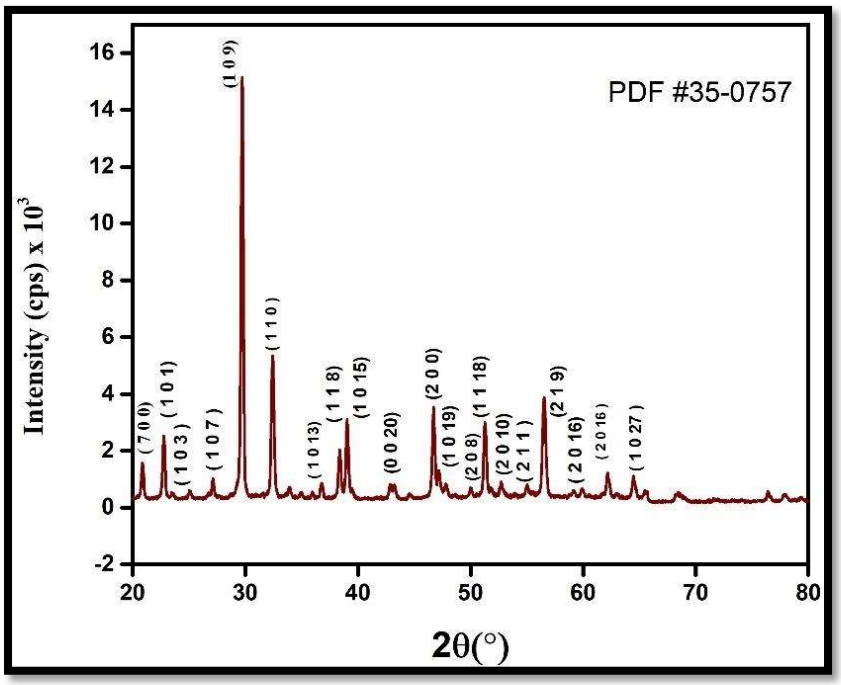

Figure 4.1 HR-XRD patterns of BBTO ceramic sintered at 950 °C for 8 h.

The crystal structure for BBTO ceramic was found to be an orthorhombic structure with space group: Fmm2. The average crystallite size of BBTO ceramic is found to be 39.24 nm, which was obtained by taking the mean of five intense XRD peaks of the ceramic using the Debye-Scherrer formula.

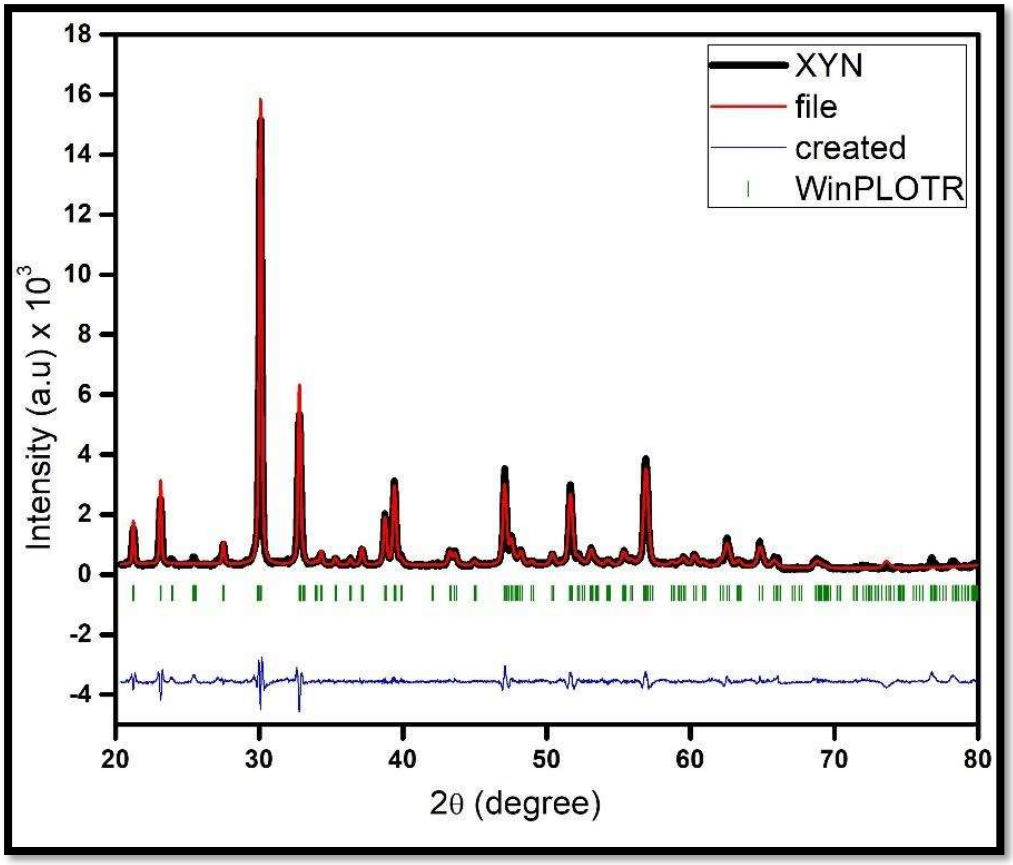

Figure 4.2 Le-Bail fitting of BBTO ceramic; black line indicates calculated data, the red line indicates experimental observed data and the blue line represents the difference between observed and calculated ($(Y_{cal} - Y_{obs})$ data.

$$D = \frac{k\lambda}{\beta \cos\theta} \tag{4.1}$$

where k taken as 0.99 refers to shape coefficient. θ, λ and β are the diffraction angle, the

wavelength of X-ray and peak width of the diffraction peak at half-maxima (FWHM) in radians,respectively.

Figure 4.2 indicates Le-Bail fitting of BBTO ceramic, which was obtained by using Fullprof software in the 2θ range from 20° to 80°. The observed data (Y_{obs}) and experimentally calculated data (Y_{cal}) indicated by red color line and black color line, respectively, overlaps precisely on each other. The low value of χ^2, Weight profile factor (R_{wp}), expected weight factor (R_{exp}), Braggs R-factor (R_B) for BBTO ceramic enlisted in table 4.1 confirms the best fitting of the XRD results(Tellier et al. 2004).

Table 4.1 Refined lattice parameters and space group of BBTO ceramic sintered at 950 °C for 8 h.

χ^2 = 3.56	R_p: 17.3	R_{wp}: 20.0	R_{exp}: 7.23
Phase			Orthorhombic
Space group			Fmm2
Lattice Parameter			a = 41.823677 Å b = 5.460870 Å c = 5.458066 Å
Angle			α = ***β*** = γ = 90°
Bragg R-factor			1.106
RF-factor			0.9969

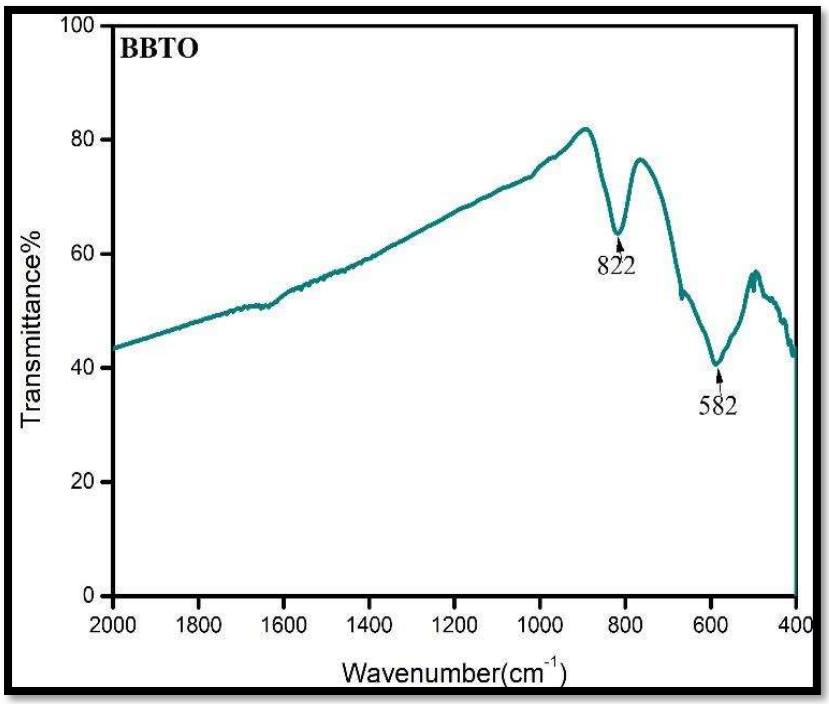

Figure 4.3 FT-IR spectra of BBTO ceramic.

Figure 4.3 depicts the FTIR spectra of the BBTO ceramic sintered at 950 °C for 8 h, recorded in 500–1500 cm^{-1} frequency range. Bands appear at 822 and 582 cm^{-1} are associated with metal-oxides bonds. The peak observed around 550 cm^{-1} is the characteristic peak of (Ti-O) bond vibration(Sun et al. 2007; Kumar et al. 2018), whereas the peak near 822 cm^{-1} is as a result of stretching vibration of Bi–O bond (Hou et al. 2011).

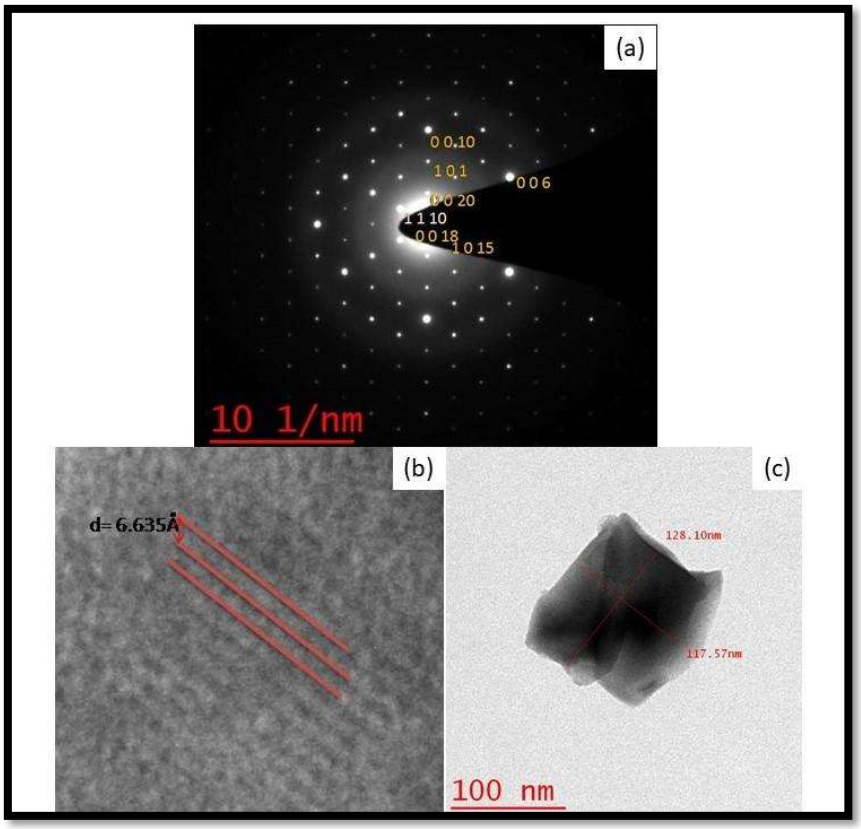

Figure 4.4 (a) SAED patterns (b) HR-TEM images showing d spacing, and (c) Bright Field TEM Images of BBTO ceramic.

In figure 4.4(a) we can observe Selected area diffraction (SAED) pattern of the single crystal of BBTO ceramic having distinct bright spot patterns corresponding to planes (0 0 20), (1 1 10), (1 0 15), (0 0 6), (1 0 1) and (0 0 10). High-resolution imaging by TEM is displayed in figure 4.4(b), it exhibits inter-planer spacing d = 6.63 Å of the corresponding planes of BBTO ceramic. Bright field TEM images of the BBTO ceramic sintered at 950 °C for 8 h is shown in figure 4.4(c) confirms the orthorhombic structure of the ceramic as concluded by HR-XRD analysis. The mean particle size observed is 122 ±2 for BBTO ceramic. The particle size obtained by TEM analysis outsize the average crystallite size measured by XRD results. The explanation of

this can be accredited to the formation of particles with the combination of few crystallites. The zone axis of the diffraction pattern between (0 0 20) and (1 1 10) planes is obtained as [$\overline{20}$ 20 0]. The planes observed in SAED pattern and HR-TEM are in agreement with XRD, which supports the orthorhombic nature of the BBTO ceramic.

The surface morphology was observed on the gold-coated surface is depicted in figure 4.5(a) reveals the presence of pellet-like grains separated by grain boundaries. The average grain size of BBTO is calculated using ImageJ software and found to be 447.27 nm. SEM analysis witnesses a larger average grain size than that of crystallite size obtained from XRD measurement as the former is formed by aggregation of the latter. Figure 4.5(b) illustrate the EDX spectrum for BBTO ceramic, which reveals the presence of Ba, Bi, Ti, and O elements in BBTO ceramic, which confirms the purity of materials.

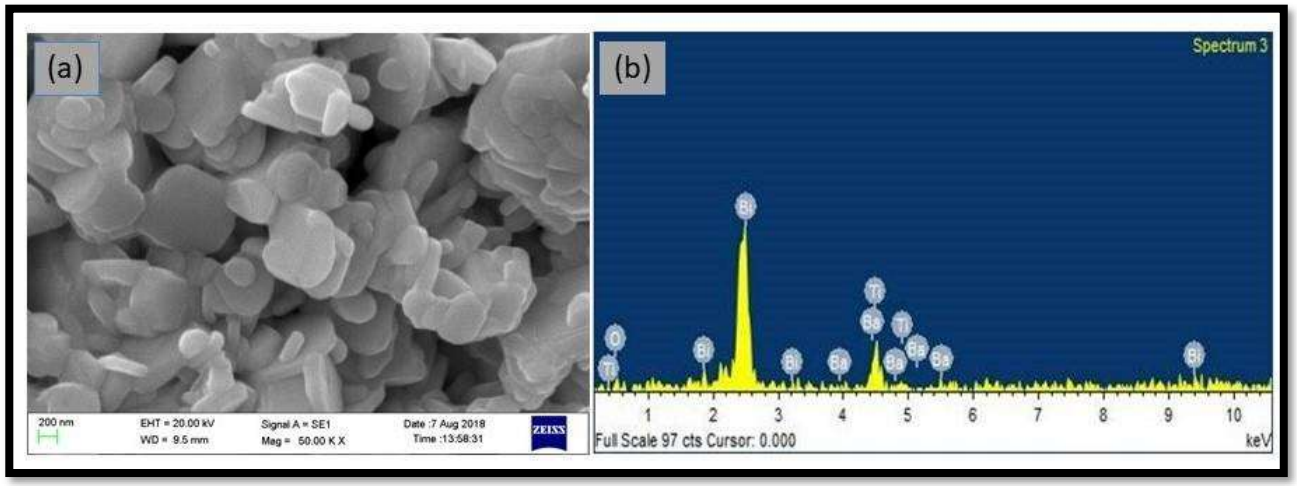

Figure 4.5 (a) SEM micrograph and (b) EDX spectra of BBTO ceramic.

AFM analysis of BBTO ceramic was done using tapping mode is depicted in figure 4.6. Histogram of grain size of particles is shown in figure 4.6(a), indicating that most of the grains

are in the size range of 0.6-0.8 um in BBTO ceramic, which is in accordance with SEM and TEM results. The distributions of particles on the surface are illustrated by a 3-dimensional AFM image on the scanned area of 20 μm x 20 μm in figure 4.6(b). Comparable grain size with clear grain boundaries is observed in 2-dimensional AFM images for BBTO ceramic is explained in figure 4.6(c). The observed value of average roughness (Ra), root mean square roughness (Rq), maximum profile peak height and maximum profile valley depth for the 3-dimensional image of BBTO ceramic are mentioned in table 4.2.

Table 4.2 Data of AFM analysis of BBTO ceramic sintered at 950 °C for 8 h.

Average roughness (Ra)	164.53 nm
Root Mean Square roughness (Rq)	184.07 nm
Maximum Profile Peak Height	325.21 nm
Maximum Profile Valley Depth	393.3 nm

The zeta potential of the material was determined by dynamic light scattering depicted in figure 4.7. The zeta potential value is a decisive particle characteristic as it can influence particle properties such as stability of particle suspension. Theoretically, distinct zeta potential values, being negative or positive, confers the stabilization of particles in suspension (Shukla et al. 2013 Apr). The same electric charge on particles creates the electrostatic repulsion between them which prevents their aggregation and sedimentation (Feng and Huang 2001). In the present study, the zeta potential was −21.3, as can be seen in figure 4.6. The negative value of zeta potential indicates the formation of the stable ceramic particles. (polydispersity index [PDI] = 1

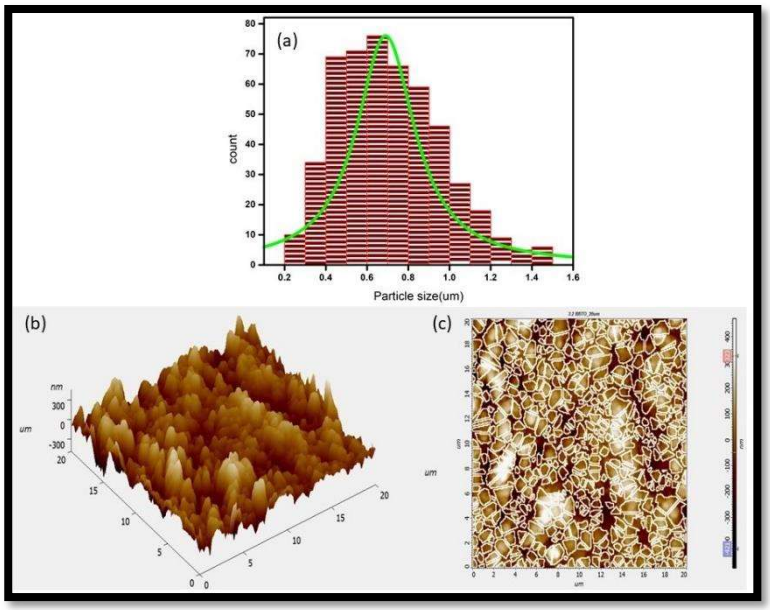

Figure 4.6 (a) Histogram graph for the particle size distribution, (b) 3-D for surface roughness and (c) 2-D watershed images for grain boundary of BBTO ceramic.

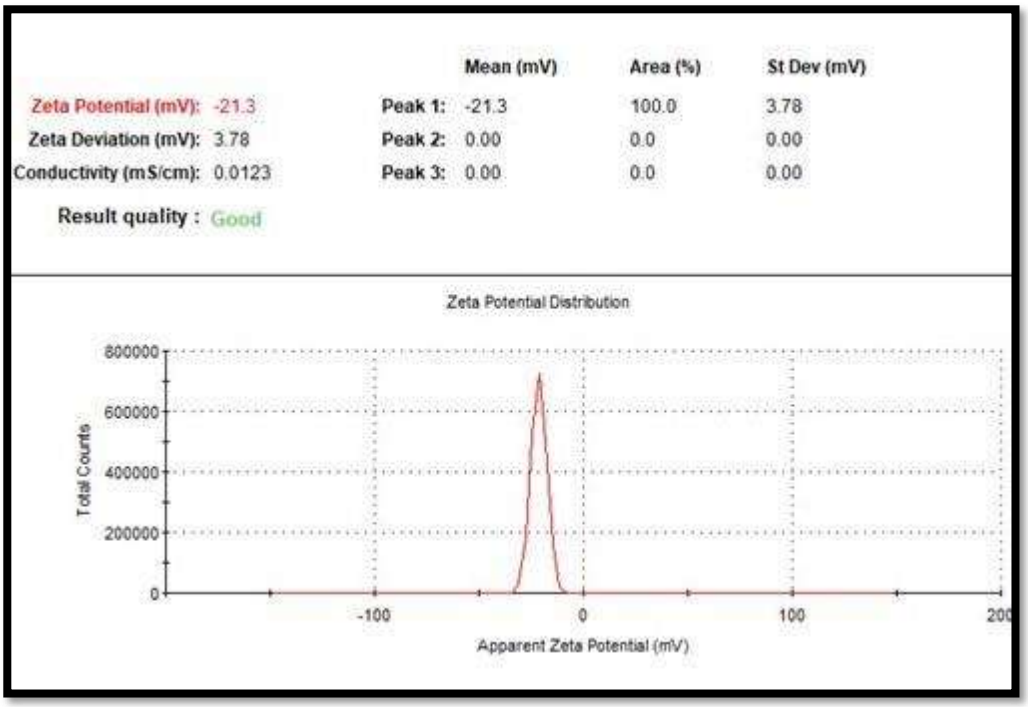

Figure 4.7 Zeta potential distribution of BBTO ceramic

To acquire information regarding the oxidation state of individual elements present in the BBTO ceramic and their electronic environment, X-ray photoelectron spectroscopic (XPS) analysis was conducted (Bantawal and Krishna Bhat 2018). The C1s peak at 284.6 eV was taken as a reference for the correction of the binding energies for specimen surface charge obtained from the XPS analysis (Singh et al. 2020). The high-resolution XPS spectrum of the BBTO ceramic is portrayed in figure 4.8(a)–(d). The presence of elements such as titanium, bismuth, oxygen, and barium in the ceramic was confirmed. Figure 4.8(a) reveals that the Ti 2p high-resolution XPS spectrum can be deconvoluted into three peaks. Among the three peaks, two are the characteristic peaks of Ti(IV), the peak present at 457.5 eV is due to Ti $2p_{3/2}$ while the peak at 463.5 eV is due to Ti $2p_{1/2}$. The third peak at 465.9 eV is characteristic of Bi $4d_{3/2}$ binding energies. Broad hump in the vicinity of 464.5 eV is witnessed as the peaks of Ti 2p1/2 and Bi 4d3/2 are partially overlapped (Chu et al. 2002; Hou et al. 2013). The existence of Bi^{+3} is confirmed by the High-resolution XPS spectra of bismuth shown in figure 4.8(b). The spectra can be deconvoluted into two distinct peaks. One at 159.1 eV binding energies is due to Bi $4f_{5/2}$ and other at 164.5 eV is attributable to Bi $4f_{7/2.}$ (Hou et al. 2013; Zhao et al. 2019).

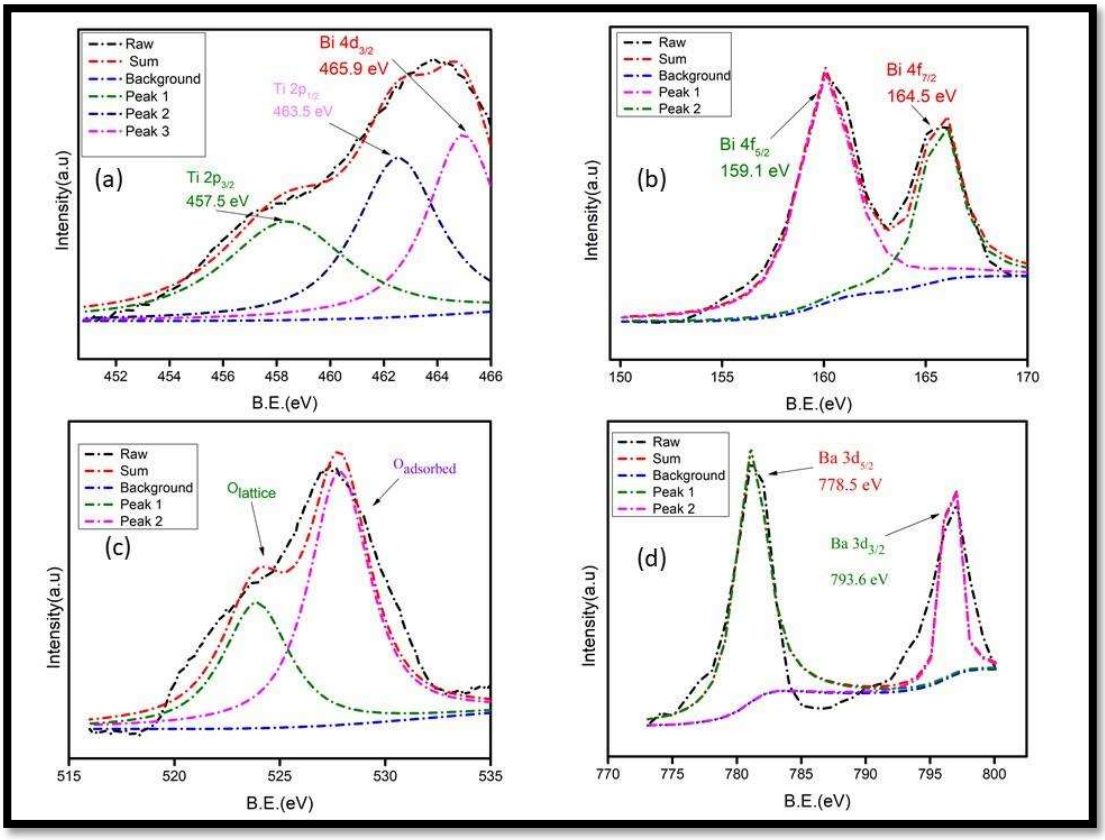

Figure 4.8 (a)–(d) High-resolution XPS spectra of the BBTO ceramics.

An asymmetric and wide spectrum of O 1s is noticeable from figure 4.8(c), surmising the existence of varied chemical state of O in the ceramic. This broad O1s spectrum is deconvoluted into two components: lattice oxygen species ($O_{lattice}$) at 524.5 eV binding energy and surface adsorbed oxygen ($O_{adsorbed}$) species around binding energy 530.0 eV. A higher ratio of concentration oxygen species adsorbed ($O_{adsorbed}$) at the surface to lattice oxygen ($O_{lattice}$) would aid in the enhancement of catalytic activity (Arandiyan et al. 2013; Hou et al. 2013). In figure 4.8(d), deconvolution of the spectrum gives two peaks at 793.65 eV and 778.35 eV binding energies that could be attributed to the splitting of the spin states Ba $3d_{3/2}$ and Ba $3d_{5/2}$, respectively (Panchal et al. 2017).

4.5 Magnetic studies

All the constituents of the ceramic, i.e., Bi, Ba, TiO_2, are diamagnetic, and therefore, ceramic is also expected to be diamagnetic (Delekar et al. 2012). It is also confirmed experimentally by the plot of measured magnetization versus applied magnetic field (M-H) curve at different temperatures as illustrated in figure 4.9(a) for BBTO ceramic using Superconducting Quantum Design MPMS Magnetometer Interference Device (SQUID) observed from 5 K to 300 K at ±2 T for. It is well lucid from the figure that magnetic nature is oppressed by diamagnetism.

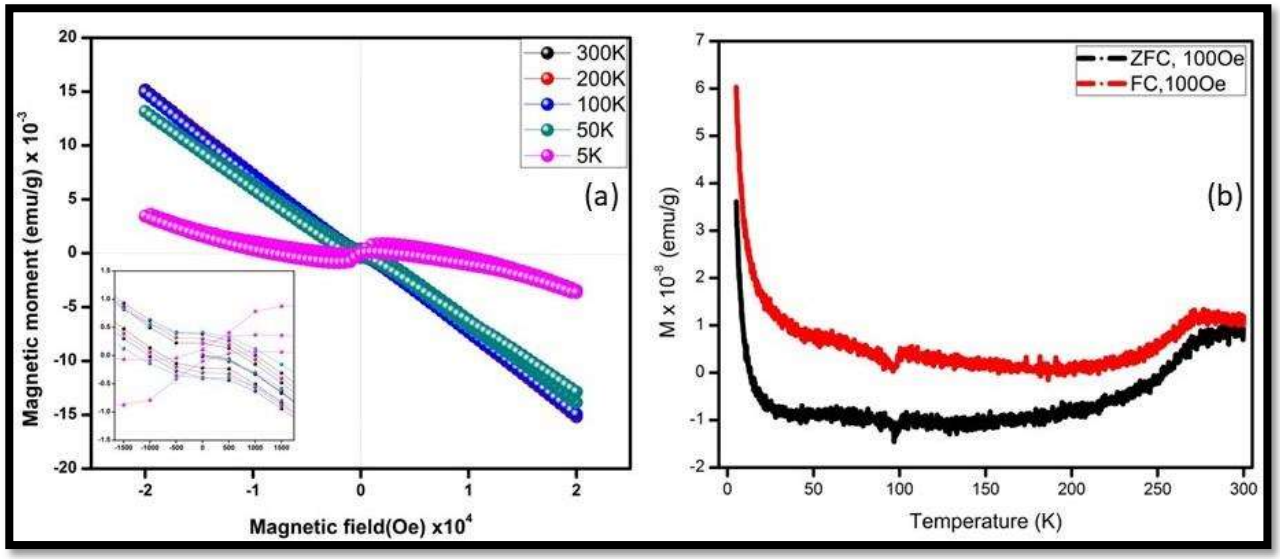

Figure 4.9 (a) M-H hysteresis loop from 5 K to 300 K and (b)Temperature-dependent ZFC and FC at H = 100 Oe for BBTO ceramic.

.Howbeit a small loop of ferromagnetism is observed at a very low temperature of 5 K, this shift can be credited to spin flop, which caused due to reversal of magnetic superlattices and their orientation is oppositely aligned with the magnetic field (May et al. 2014; Bhattacharya et al.).

Variation of magnetization as a function of temperature at a constant applied field of 100 Oe was analyzed during the cooling process up to 5 K from room temperature (300 K). From figure 4.9(b), it is observed that a substantial difference exists between the magnetization curve of zero

field cooled (ZFC) and field cooled (FC) for BBTO ceramic at lower temperatures. This ample gap implies that material is a frustrated spin system (Sultan et al. 2015). Average interactions like thermally induced disorders, ferromagnetism, anti-ferromagnetism and canted spins structure generate frustrated spin system. Peaks observed at 80 -100 K in both FC and ZFC at 100 Oe is due to magnetic phase transition (Biswal et al.). An inverse relation of magnetization and temperature is evident from figure 4.9(b) as both FC and ZFC magnetization increases with decreasing temperature. However, increase at a lower temperature is exponential and this feature is explained by Monte Carlo; according to him, alignment of disordered spins ensue along the normal axis to the material surface at lower temperature insinuating a net exponential increase in the magnetic moment (J. Rawat et al. 2007; Jagdish Rawat et al. 2007; Chakrabarti et al. 2013).

4.6 Impedance studies

It is an effective approach for assessing the electrical properties of polycrystalline materials and determining how their microstructures govern them. It also includes information regarding the coexistence of multi-polarization and their relaxation processes. The pragmatic participation of electrode interface, grain boundaries and grains to the total resistance and capacitance can also be estimated (Wang et al. 2017). Three semicircular arcs attained in complex impedance spectroscopy plot [(Z") imaginary part of impedance versus (Z') real part of impedance] signifies their contributions.

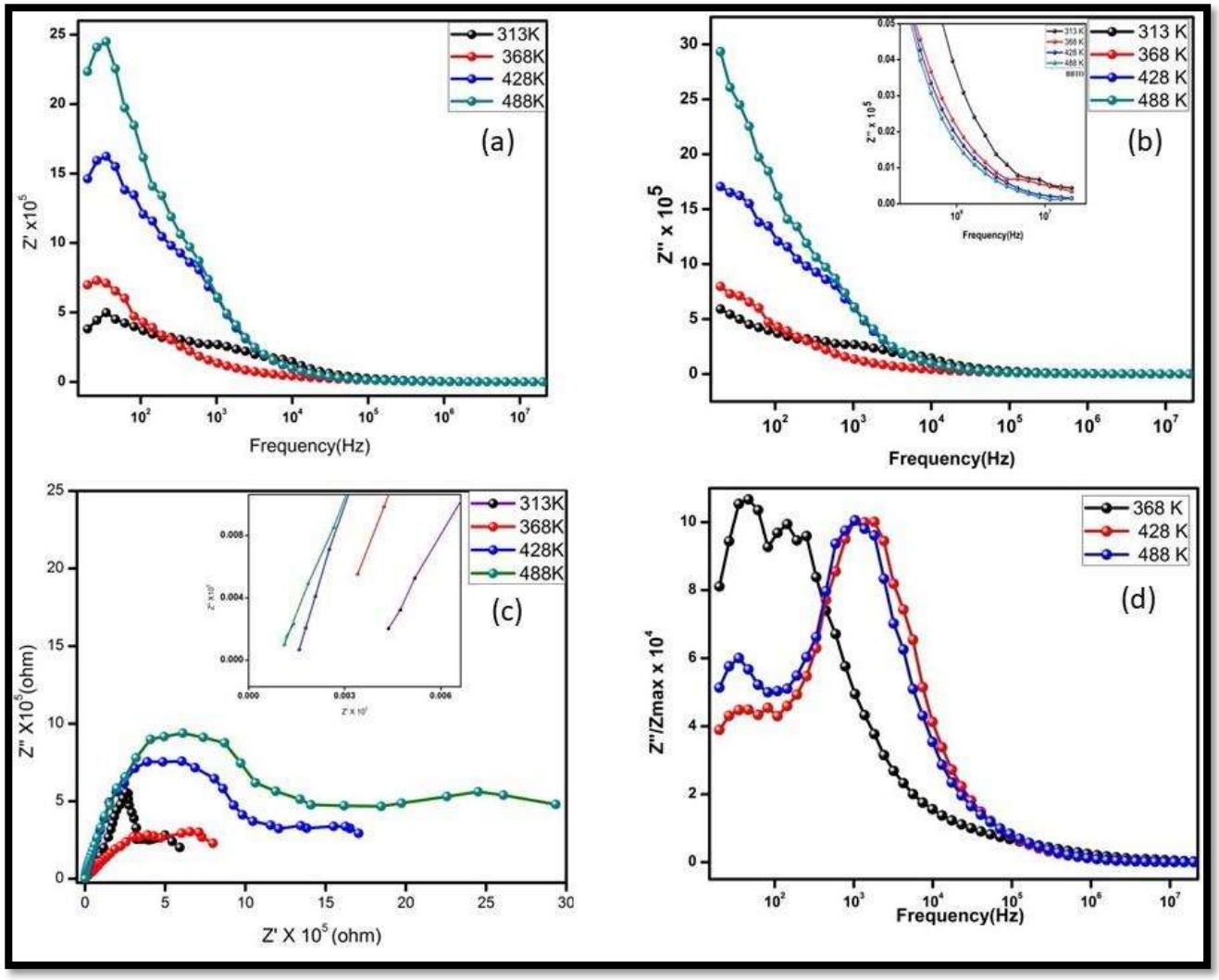

Figure 4.10 (a) represents plot of the real part of impedance as a function of frequency at different temperatures and (b) Plot of the imaginary part of impedance as a function of frequency at different temperatures. (c) Complex impedence spectroscopy in a range of temperature (313 K-488 K) for BBTO ceramic and the inset is exhibiting an enlarged view of the higher frequencies. (d) Normalized imaginary part of impedance as a function of frequency for BBTO ceramic.

Variation of the real part of impedance and imaginary part of impedance at few selected temperatures are illustrated in figure 4.10(a) and figure 4.10(b), respectively. Both the plots exhibited similar behavior, a decrease in the values of Z' and Z'' as there was a rise in frequency, implying an increase in ac conductivity (Thomas et al. 2017). The existence of relaxation peaks

can also be seen in the plots, the reason for the occurrence of relaxation peaks at the lower frequency region is attributed to the contribution of the electrode, while grain boundary effects cause relaxation at the higher frequency region. Figure 4.10(c) shows the complex impedance spectroscopy of BBTO ceramic sintered at 950^0 C for 8 h and only two semicircular arcs are evident due to the contribution of grain boundaries and electrode surface effects. The inset in the figures exhibits data at a higher frequency and on extrapolation of arc on Z′ axis, the intercept does not find to pass through origin, implying the presence of another arc in higher frequency region that is beyond the range of measurement. The intercept obtained at Z′ axis is the resistance offered by grains (R_g). The resistance exerted by grain boundaries (R_{gb}), the grain capacitance (C_g) and grain boundary capacitance (C_{gb}) were calculated and mentioned in table 4.3. The impedance offered by the grains and grain boundaries is expressed by the following equation (Kumar et al. 2018).

$$Z^* = \frac{1}{R_g^{-1}+i\omega C_g} + \frac{1}{R_{gb}^{-1}+i\omega C_{gb}} = Z' - iZ'' \quad (4.2)$$

Where, $$Z' = \frac{R_g}{1+(\omega R_g C_g)^2} + \frac{R_{gb}}{1+(\omega R_{gb} C_{gb})^2} \quad (4.3)$$

And $$Z'' = R_g\left[\frac{\omega R_g C_g}{1+(\omega R_g C_g)^2}\right] + R_{gb}\left[\frac{\omega R_{gb} C_{gb}}{1+(\omega R_{gb} C_{gb})^2}\right] \quad (4.4)$$

where, R_g is grain resistance, R_{gb} is grain boundary resistance, C_g and C_{gb} are the capacitance of grain and grain boundary, respectively and ω is the angular frequency. The repressions of grain's contribution were due to the larger contribution of grain boundaries. It is observed from the table 4.3 that the value of grains for BBTO ceramic is lower than that of grain boundaries, which justifies the semiconducting nature of grains with insulating grain boundaries, as explained by the Inter-barrier layer capacitance (IBLC) mechanism.

Table 4.3 The resistance and capacitance exerted by grain boundaries and grains of BBTO ceramic at a few selected temperatures.

Temperature (K)	R_g (Ω)	C_g (pF)	R_{gb}(Ω) x 10^5	C_{gb} (pF)
313	438.37	0.182	16.124	0.1323
368	340.38	0.234	10.45	0.0111
428	158.32	0.503	4.657	0.148
488	140.25	0.568	3.204	0.122

Suppression and shifting of relaxation peaks occurring at higher frequency regions provide evidence for the existence of temperature dependent Maxwell-Wagner dielectric relaxation phenomenon as can be seen from the inset of figure 4.10(b).

Variation of the normalized imaginary part of impedance (Z″/Z″max) with frequencies at few temperatures in BBTO ceramic can be seen in figure 4.10(d). Single relaxation peaks are evident in each case. At the same time, a short tail in the lower frequency range is also noticed at 368 K, which can be ascribed to the contribution of electrode and grain boundary that offers more considerable resistance (Zhang et al. 2018). Single relaxation peaks are witnessed to shift slightly towards higher frequency region as the temperature increases, this incongruity in peak frequency accredited to the movement of charge carriers to short-range indicating toward thermally activated non-Debye like relaxation phenomena (Ke et al. 2010; Thomas et al. 2017). Peaks obtained at a higher frequency and lower frequency range highlight the character of grain and grain boundaries, respectively.

Figure 4.11(a) portrays the reliance of AC conductivity on frequencies of the BBTO ceramic at few selected temperatures. Conductivity in low frequency region primarily depends on temperature on the contrary, at a higher frequency region it primarily frequency driven (Shehata and Abdelhady 2018). Hitherto it has been validated that frequency driven ac conductivity is akin for both disordered or ordered state of solids, as it is mainly an outcome of

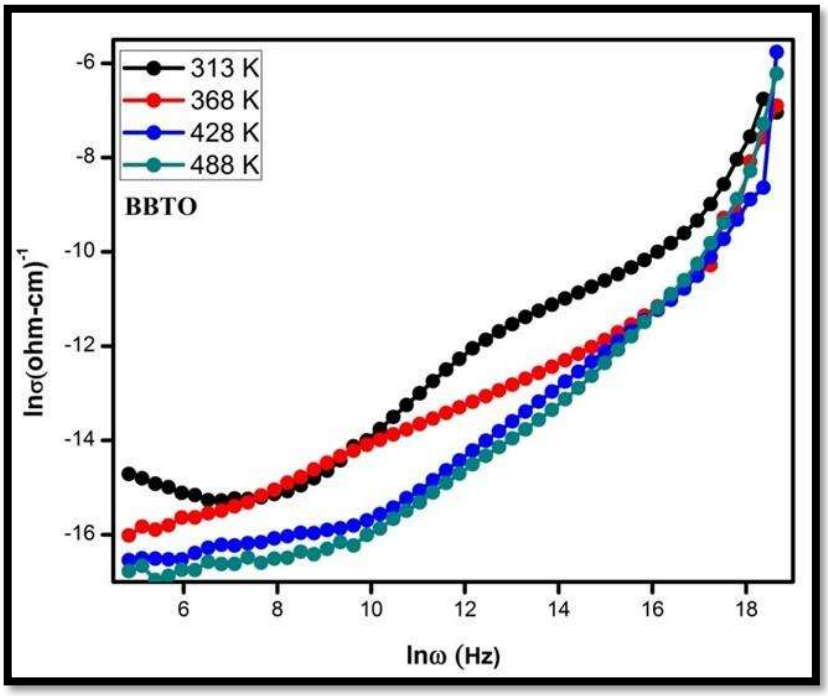

Figure 4.11 Frequency dependent AC conductivity at different temperatures for BBTO ceramic.

hopping charge carrier conduction, which is ineffectual at lower frequency range. The movement of charge carriers is assumed to be in discontinuous jumps, "hopping" from one well defined localized site to another within the solids.

It can be seen in figure 4.11 that there is a portion of the plot where conductivity shows a monotonical increase as a function of frequency, which fits appropriately by "Joscher's universal power law".

$$\sigma_{ac} \propto \omega^{n} \tag{4.5}$$

Where the power-law exponent is denoted by n, whose value lies within $0 < n < 1$ range. The values of the power-law exponent obtained by fitting plots at a few selected temperatures are shown in table 4.4 for BBTO ceramic.

Table 4.4 The value of power-law exponent found for BBTO ceramic from the plots shown in figure 4.11 at a few selected temperatures.

Temperature	313 K	368 K	428 K	488 K
BBTO ceramic	0.39	0.42	0.66	0.67

These values validate the presence of Maxwell-Wagner effects induced by a thin oxide layer on the electrode at the same time excludes the existence of Debye-type relaxation as for such relaxation, the values of the power-law exponent should be around 2 (Jonscher 1972).

4.7 Dielectric Studies

The dependency of dielectric constant for BBTO ceramic on the frequency at four different temperatures is displayed in figure 4.12(a).

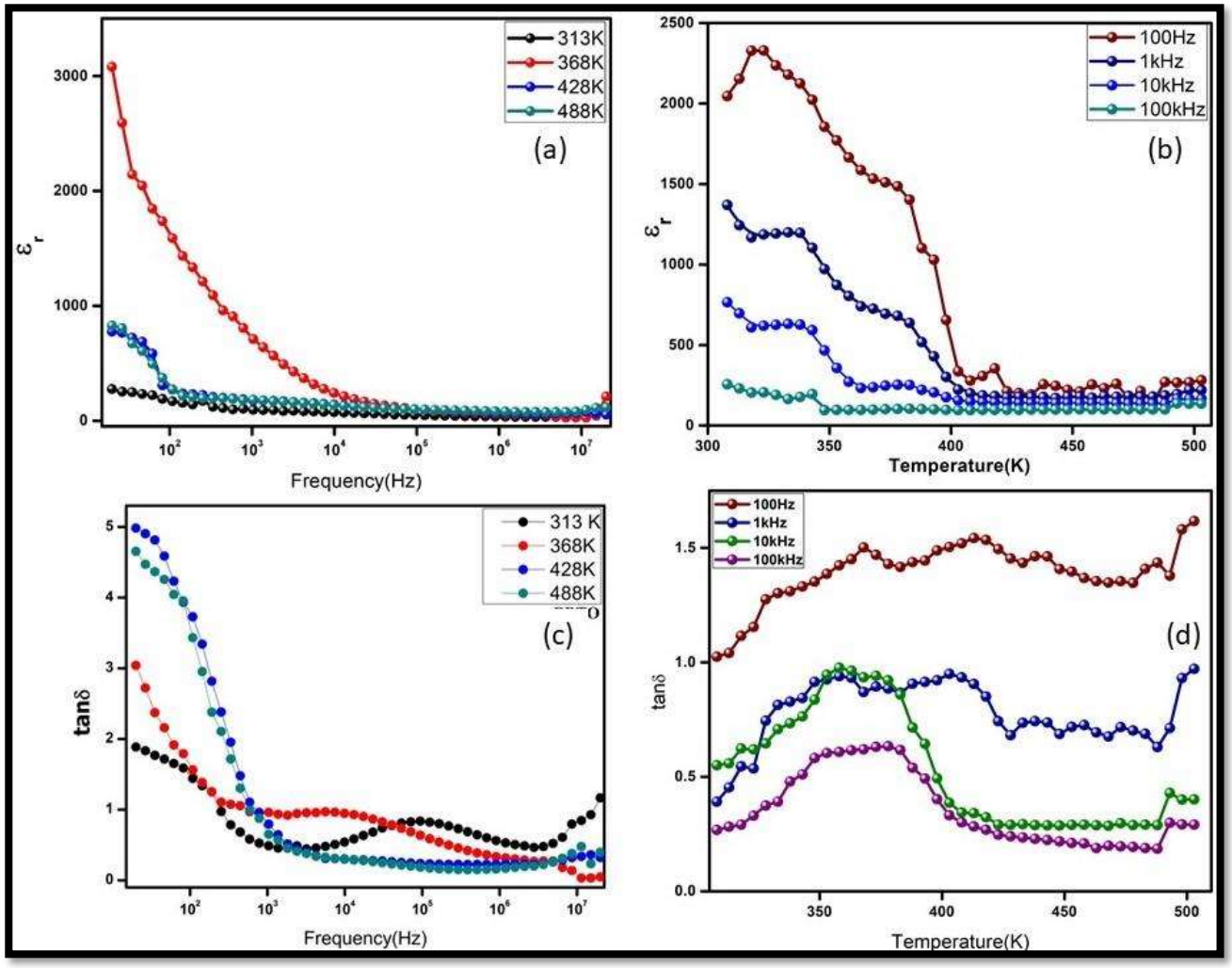

Figure 4.12 (a) Dielectric constant (ε_r) as a function of frequency; (b) Dielectric constant (ε_r) as a function of temperature for BBTO ceramic; (c) Dielectric loss (tanδ) as a function of frequency; (d) Dielectric loss (tanδ)) as a function of temperature for BBTO ceramic.

It is well evident from the figure that with increasing frequency, the value of the dielectric constant decreases. Although a steep fall in the values is witnessed in low frequency range, it can be ascribed as, at the interface, space charge gets accumulated, ensuing the polarization of the ionic medium. Conversely, at higher frequency region, rapid switch of field recurs, which prevent the accumulation of space charge at interface. Thus, almost constant value of the

dielectric constant is perceived (Sharma et al. 2014). The value of dielectric constant at 100Hz and 368 K was found to be 3081 for BBTO ceramic.

Figure 4.12(b) demonstrates the dependence of dielectric constant on the temperature at a few specific frequencies for BBTO ceramic. As expected for a typical ferroelectric material, BBTO ceramic also reach maxima then decreases, the temperature corresponding to this maxima is referred to as Curie temperature, where the ferroelectric phase transforms to paraelectric phase. Phase transitions are also seen to vary slightly with frequency, which unveils the existence of diffuse phase transition verifying the relaxor ferroelectric nature of the material. The explanation of this shift is supported by Modified Curie-Weiss law (Zn et al. 2017).

$$\frac{1}{\varepsilon} = \left(\frac{T - T_m}{C}\right)^{\gamma} \quad . \tag{4.8}$$

ε symbolizes Dielectric constant; T is temperature; T_m is the shift in maximum temperature, which correspond to maxima; C is the Curie temperature.

If γ = 0, then phase transition is frequency independent. However, if γ> 0, then it means that transition temperature is frequency driven and it exhibits diffuse behavior.

Figure 4.12(c) illustrates the effect of frequency on dielectric loss (tan δ) at four different temperatures. The inverse behavior of dielectric loss was observed to decrease with increasing frequency because energy dissipation occurs as polarization lags behind the applied electric field frequency(Yadava et al. 2017; Rani et al.). The occurrence of relaxation peaks is also evident, which arises from the resonance of the hopping frequency of charge carriers with the frequency of applied field (Delekar et al. 2012; Murugesan et al. 2015). The dielectric loss obtained for BBTO ceramic at 313 K and 100 Hz is 1.89. Figure 4.12(d) portrays the plots of dielectric loss (tan δ) with the temperature at four different frequencies. It is observed that the value of

dielectric loss (tan δ) increases first and then attains maximum value, from where it decreases swiftly, more lucid at lower frequencies. Such behavior again confirms the occurrence of Maxwell Wagner relaxation (Sharma et al. 2014).

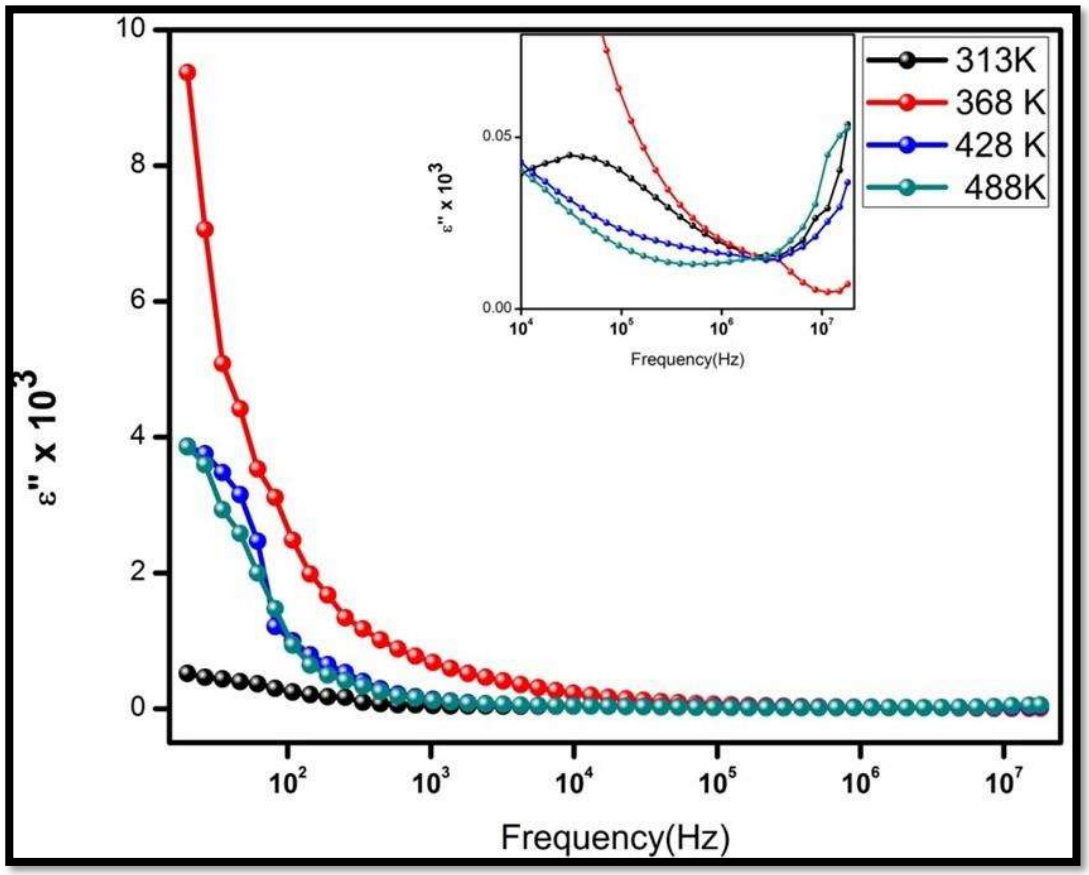

Figure 4.13 The imaginary part of dielectric constant (ε") as a function of frequency for BBTO ceramic.

The validation for the relaxor behavior in BBTO ceramic is confirmed by analysis of the imaginary part of dielectric constant (ε"). Its variation with frequency is depicted in figure 4.13. The massive value of ε" is measured at a lower frequency, which declines steeply with the rise in frequency (Wang et al. 2017). The infection point obtained in this plot is similar to the infection point in the plot Z" versus frequency shown in figure 4.10(b), strongly indicating the existence of

Maxwell-Wagner relaxation (Sharma et al. 2015). It is obvious from the inset of figure 4.13 that relaxation exists even in the higher frequency range that once again affirms the occurrence of Maxwell-Wagner relaxation. Maxwell-Wagner equation explains the relationship of ε" with frequency, as follows-:

$$\varepsilon'' = \frac{1}{\omega c_0 \left(R_{gb}+R_g\right)} \frac{1-\omega^2\tau_{gb}\tau_g+\omega^2\tau\left(\tau_{gb}+\tau_g\right)}{1+\omega^2\tau^2} \quad (4.9)$$

where,

$$\tau_g = C_g R_g \; and \; \tau_{gb} = C_{gb} R_{gb} \quad (4.10)$$

$$\tau = \frac{\tau_{gb}R_g+\tau_g R_{gb}}{R_{gb}+R_g} \; ; C_0 = \varepsilon_0 \frac{A}{t} \quad (4.11)$$

Where, τ - relaxation time; ω - angular frequency; A- area of the cylindrical pellets; t - thickness of the cylindrical pellet; subscript g and gb symbolizes grains and grains boundaries, respectively(Wang et al. 2017).

4.8 Bandgap Analysis

Bandgap analysis is imperative for deducing the mechanism of photocatalysis and concluding which segment of solar radiation is functional for the procedures. The data from UV-DRS was utilized to construct Tauc's plot for the estimation of bandgap using the following relation.

$$(\boldsymbol{\alpha h\nu})^{1/n} = \left(\boldsymbol{h\nu - E_g}\right) \quad (4.12)$$

In equation 12, α is the molar absorption coefficient, and the value of exponent 1/n is 2 for direct transition (Viezbicke et al. 2015). The intercept of the linear fit on the x-axis(hν) construes the optical band gap (Eg), which corresponds to 3.1 Ev, as can be seen in figure 4.14. This bandgap suggests the use of UV radiation for photocatalysis(David et al. 2018).

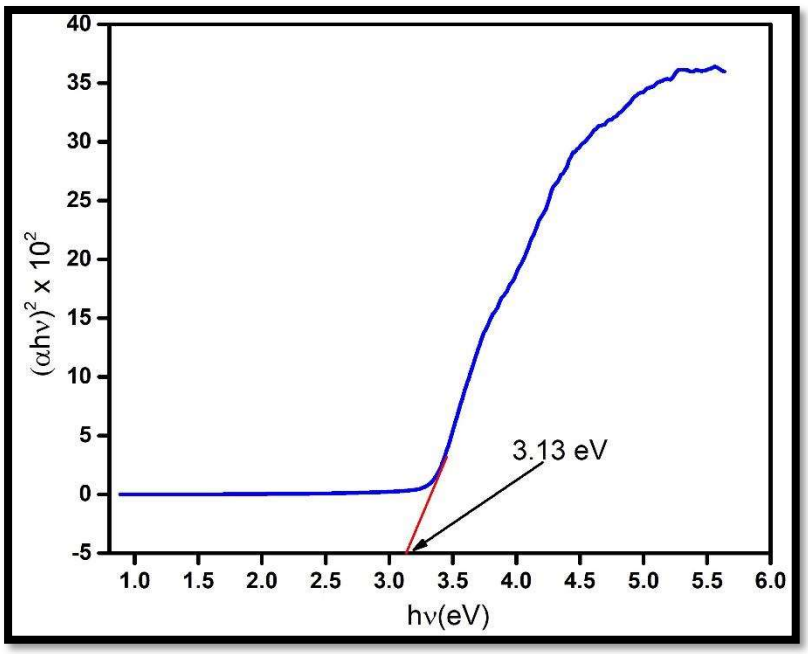

Figure 4.14 Tauc's Plot for BBTO ceramics.

4.9 BET Surface Area Analysis

The isotherms of nitrogen adsorption-desorption have been employed to attain the specific surface area of BBTO ceramic and its distribution of pore size. The isotherm shown in figure 4.15 exhibits a hysteresis loop(distorted) at a relative pressure (P/P_o) close to unity is, revealing the existence of a mesoporous structure, which can be categorized as type IV according to IUPAC classification with characteristic H3-shaped hysteresis loops (Kruk and Jaroniec 2001). The H3 hysteresis loop corresponds with pellets-like grains forming slit-like pores, the same can be verified by SEM analysis(Xiang et al. 2011). The specific surface area of BBTO ceramic obtained with the analysis is 1.325 m^2g^{-1}. The inset of the figure 4.15 displays the BJH pore size distribution curve acquired from the desorption branch. The range BJH pore size distribution is

obtained wide encompassing macropores as well as mesopores. However, the maximum pores are in the range of 10~25 nm, indicating the predominance of mesopores. Pore-diameter of mesoporous pores facilitates capillary condensation phenomena as they are much capacious than the size of adsorbate molecules, thus augmenting the catalytic activity (Kim and Ehrman 2009; Hall et al. 2012).

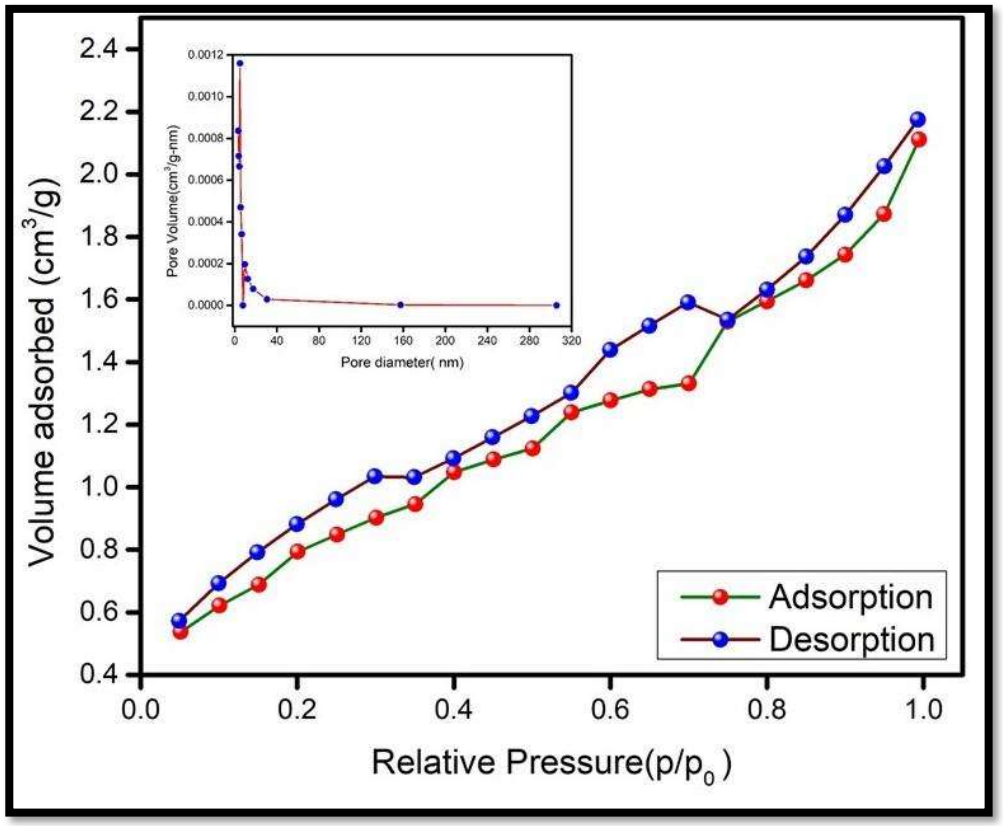

Figure 4.15 N_2 adsorption-desorption isotherms and the inset corresponding to pore-size distribution curves for BBTO ceramic.

4.10 Photocatalytic Efficiency:

Evaluation of the photocatalytic activity of BBTO ceramic was done by the degradation of organic dye, a common water pollutant, under solar radiation. This activity is well illustrated in

figure 4.16(a), which depicts that the BBTO photocatalyst in 60 minutes of the time period degrades up to 80% of RhB dye. In figure 4.16(b), the kinetic plot of $\ln(A_t/A_0)$ for degradation of RhB versus irradiation time is shown, the experimental data was obtained to fit well with 1st order kinetics and along with it, it can be seen that no significant degradation in the absence of either the BBTO ceramic or the solar radiation was observed. The correlation coefficient (R^2) and k_{app} was found to 0.9920 and 0.0279 $min^{-1,}$ respectively, for the photodegradation of RhB with BBTO.

In the photocatalytic experiment involving the degradation of many organic recalcitrant, a key role is played by various active species, like hydroxyl radical ($OH^{\cdot}$), superoxide radical ($O_2^{\cdot-}$), and (h^+). To release the active species acting in the present case, a scavenging operation for these species was performed. The scavengers such as p-benzoquinone (PBQ), isopropyl alcohol (IPA), and potassium iodide (KI) were utilized to trap active species $O_2^{\cdot-}$ radicals, $OH^{\cdot}$ radicals, and holes (h^+), respectively (Singh et al. 2020 Jun 5). The outcome of scavenging experiments for BBTO ceramic is displayed in 4.16(c). The graph shows that PBQ substantially inhibits RhB degradation in comparison to other trapping agents. KI also has a negative effect on the photodegradation of RhB, while the addition of IPA displays a minimum negative impact over the degradation of RhB. Therefore, $O_2^{\cdot-}$ and h^+ are inferred to be the major reactive species in order of $O_2^{\cdot-} > h^+ > OH^{\cdot}$, generated in the photocatalytic reaction.

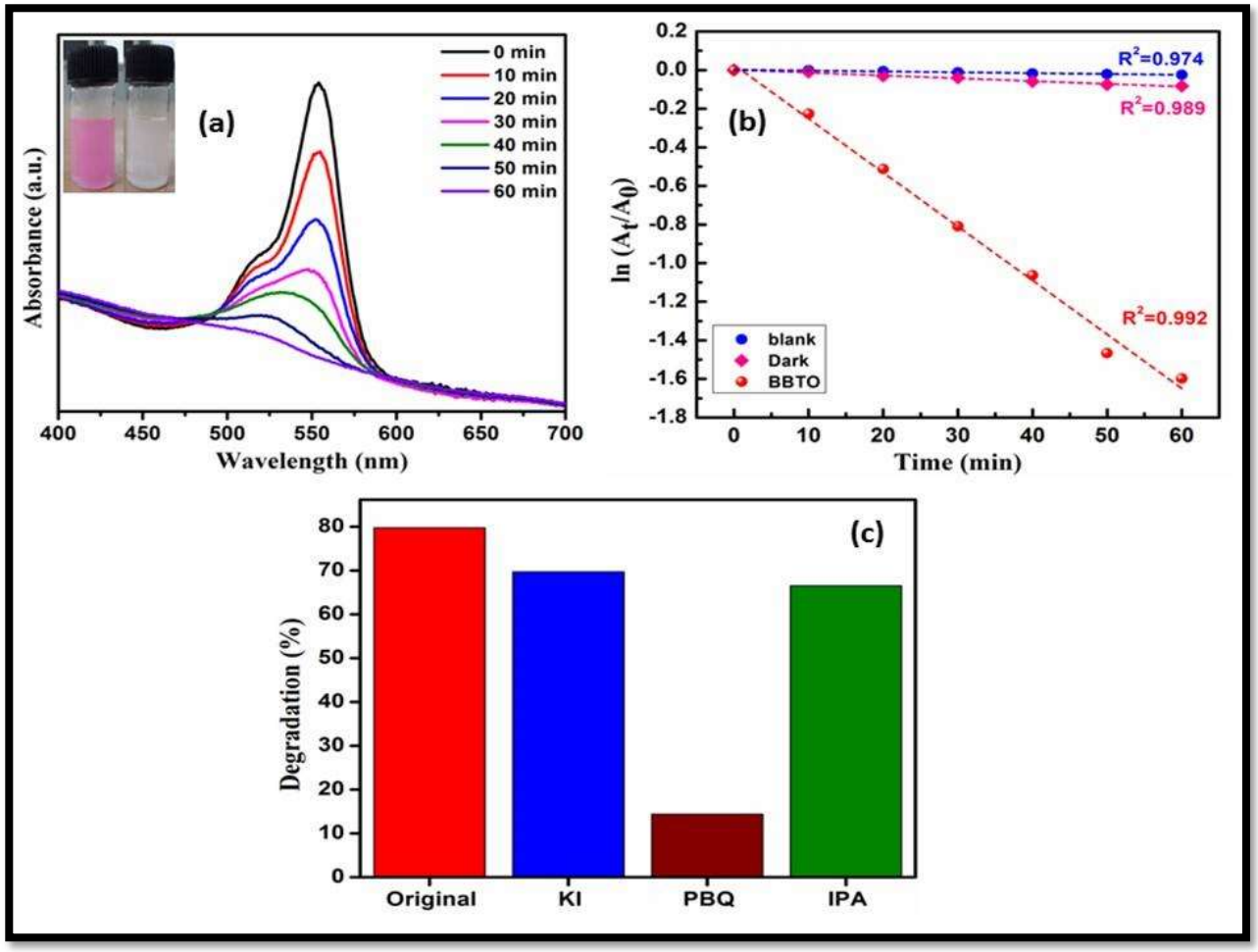

Figure 4.16 (a) UV-Vis absorbance spectra of RhB degradation by BBTO photocatalyst, (b) Kinetic first-order kinetic plot for RhB degradation by BBTO, (c) percentage degradation of RhB with different scavengers.

4.11 References-

Arandiyan H, Dai H, Deng J, Liu Y, Bai B, Wang Y, Li X, Xie S, Li J. 2013. Three-dimensionally ordered macroporous La0.6Sr0.4MnO3 with high surface areas: Active catalysts for the combustion of methane. Journal of Catalysis. 307:327–339. doi:10.1016/j.jcat.2013.07.013.

Bantawal H, Krishna Bhat D. 2018. Hierarchical Porous Batio3 Nano-Hexagons as A Visible Light Photocatalyst. IJET. 7(4.5):105. doi:10.14419/ijet.v7i4.5.20022.

Benedek NA, Rondinelli JM, Djani H, Ghosez P, Lightfoot P. 2015. Understanding ferroelectricity in layered perovskites: new ideas and insights from theory and experiments. Dalton Trans. 44(23):10543–10558. doi:10.1039/C5DT00010F.

Bhattacharya S, Maiti R, Sen MB, Saha SK, Chakravorty D. Anomalous enhancement in the magnetoconductance of graphene / CoFe 2 O 4 composite due to spin – orbit coupling. doi:10.1088/0022-3727/48/43/435002.

Biswal S, Bhaskaram DS, Govindaraj G. Graphene oxide : structure and temperature dependent magnetic characterization Graphene oxide : structure and temperature dependent magnetic characterization.

Chakrabarti K, Sarkar B, Ashok VD. 2013. Interfacial magnetism and exchange coupling in BiFeO 3 – CuO nanocomposite. doi:10.1088/0957-4484/24/50/505711.

Chu M-W, Ganne M, Caldes MT, Brohan L. 2002. X-ray photoelectron spectroscopy and high resolution electron microscopy studies of Aurivillius compounds: Bi 4- x La x Ti 3 O 12 (x= 0, 0.5, 0.75, 1.0, 1.5, and 2.0). Journal of applied physics. 91(5):3178–3187.

David TM, Wilson P, Mahesh R, Sagayaraj P, Murugesan N, Ramesh C, Seshadri H. 2018. Photocatalytic water splitting of TiO_2 nanotubes powders prepared via rapid breakdown anodization sensitized with Pt, Pd and Ni nanoparticles. Materials Technology. 33(4):288–300. doi:10.1080/10667857.2018.1433349.

Delekar SD, Yadav HM, Achary SN, Meena SS, Pawar SH. 2012. Structural refinement and photocatalytic activity of Fe-doped anatase TiO 2 nanoparticles. Applied Surface Science. 263:536–545. doi:10.1016/j.apsusc.2012.09.102.

Depan D, Misra RDK. 2014. On the determining role of network structure titania in silicone against bacterial colonization: Mechanism and disruption of biofilm. Materials Science and Engineering: C. 34:221–228. doi:10.1016/j.msec.2013.09.025.

Feng S, Huang G. 2001. Effects of emulsifiers on the controlled release of paclitaxel (Taxol®) from nanospheres of biodegradable polymers. Journal of Controlled Release.:17.

Galasso FS, Kestigan M. 2007. Bismuth Titanate, Bi $_4$ Ti $_3$ O $_{12}$. In: Murphy DW, Interrante LV, editors. Inorganic Syntheses. Hoboken, NJ, USA: John Wiley & Sons, Inc. p. 112–113. [accessed 2021 Jan 10]. http://doi.wiley.com/10.1002/9780470132616.ch24.

Girase B, Depan D, Shah JS, Xu W, Misra RDK. 2011. Silver–clay nanohybrid structure for effective and diffusion-controlled antimicrobial activity. Materials Science and Engineering: C. 31(8):1759–1766. doi:10.1016/j.msec.2011.08.007.

Hall MR, Tsang SCE, Casey SP, Khan MA, Yang H. 2012. Synthesis, characterization and hygrothermal behaviour of mesoporous silica high-performance desiccants for relative humidity buffering in closed environments. Acta Materialia. 60(1):89–101. doi:10.1016/j.actamat.2011.09.016.

Han F, Kambala VSR, Srinivasan M, Rajarathnam D, Naidu R. 2009. Tailored titanium dioxide photocatalysts for the degradation of organic dyes in wastewater treatment: A review. Applied Catalysis A: General. 359(1–2):25–40. doi:10.1016/j.apcata.2009.02.043.

Hou D, Luo W, Huang Y, Yu JC, Hu X. 2013. Synthesis of porous Bi4Ti3O12 nanofibers by electrospinning and their enhanced visible-light-driven photocatalytic properties. Nanoscale. 5(5):2028. doi:10.1039/c2nr33750a.

Hou J, Cao R, Wang Z, Jiao S, Zhu H. 2011. Chromium-doped bismuth titanate nanosheets as enhanced visible-light photocatalysts with a high percentage of reactive {110} facets. J Mater Chem. 21(20):7296. doi:10.1039/c0jm04374e.

Jonscher AK. 1972. Department of Physics, Chelsea College, Pulton Place, London S.W.6, England. Journal of Non-Crystalline Solids. 10:293–315.

Ke Q, Lou X, Wang Y, Wang J. 2010. thin films. :1–7. doi:10.1103/PhysRevB.82.024102.

Kendall KR, Navas C, Thomas JK, zur Loye H-C. 1996. Recent Developments in Oxide Ion Conductors: Aurivillius Phases. Chem Mater. 8(3):642–649. doi:10.1021/cm9503083.

Kim S, Ehrman SH. 2009. Photocatalytic activity of a surface-modified anatase and rutile titania nanoparticle mixture. Journal of Colloid and Interface Science. 338(1):304–307. doi:10.1016/j.jcis.2009.06.047.

Kruk M, Jaroniec M. 2001. Gas Adsorption Characterization of Ordered Organic−Inorganic Nanocomposite Materials. Chem Mater. 13(10):3169–3183. doi:10.1021/cm0101069.

Kumar A, Yadava SS, Gautam P, Khare A, Mandal KD. 2018. Magnetic and dielectric studies of barium hexaferrite (BaFe12O19) ceramic synthesized by chemical route. Journal of Electroceramics.:1–10. doi:10.1007/s10832-018-0146-x.

Lachheb H, Puzenat E, Houas A, Ksibi M, Elaloui E, Guillard C, Herrmann J-M. 2002. Photocatalytic degradation of various types of dyes (Alizarin S, Crocein Orange G, Methyl Red,

Congo Red, Methylene Blue) in water by UV-irradiated titania. Applied Catalysis B: Environmental. 39(1):75–90. doi:10.1016/S0926-3373(02)00078-4.

Li X, Sun Y, Xiong T, Jiang G, Zhang Y, Wu Z, Dong F. 2017. Activation of amorphous bismuth oxide via plasmonic Bi metal for efficient visible-light photocatalysis. Journal of Catalysis. 352:102–112. doi:10.1016/j.jcat.2017.04.025.

Liang Y, Wang S, Guo P. 2017. Effects of Ag on the photocatalytic activity of multiple layer TiO_2 films. Materials Technology. 32(1):46–51. doi:10.1080/10667857.2015.1116821.

Liu G, Wang L, Yang HG, Cheng H-M, (Max) Lu GQ. 2010. Titania-based photocatalysts—crystal growth, doping and heterostructuring. J Mater Chem. 20(5):831–843. doi:10.1039/B909930A.

Liu Y, Zhang M, Li L, Zhang X. 2014. One-dimensional visible-light-driven bifunctional photocatalysts based on Bi4Ti3O12 nanofiber frameworks and Bi2XO6 (X=Mo, W) nanosheets. Applied Catalysis B: Environmental. 160–161:757–766. doi:10.1016/j.apcatb.2014.06.023.

Ma Z, Ren L, Liu R, Yang K, Zhang Y, Liao Z, Liu W, Qi M, Misra RDK. 2015. Effect of Heat Treatment on Cu Distribution, Antibacterial Performance and Cytotoxicity of Ti–6Al–4V–5Cu Alloy. Journal of Materials Science & Technology. 31(7):723–732. doi:10.1016/j.jmst.2015.04.002.

Maradudin AA. SIZE DRIVEN PHASE TRANSITION IN FERROELECTRIC PARTICLES Y.G. Wang, W.L. Zhong and P.L. Zhang. :4.

May AF, McGuire MA, Sales BC. 2014. Effect of Eu magnetism on the electronic properties of the candidate Dirac material EuMnBi 2. Phys Rev B. 90(7):075109. doi:10.1103/PhysRevB.90.075109.

Misra RDK, Girase B, Depan D, Shah JS. 2012. Hybrid Nanoscale Architecture for Enhancement of Antimicrobial Activity: Immobilization of Silver Nanoparticles on Thiol-Functionalized Polymer Crystallized on Carbon Nanotubes. Adv Eng Mater. 14(4):B93–B100. doi:10.1002/adem.201180081.

Moure A. 2018. Review and Perspectives of Aurivillius Structures as a Lead-Free Piezoelectric System. Applied Sciences. 8(1):62. doi:10.3390/app8010062.

Murugesan C, Sathyamoorthy B, Chandrasekaran G. 2015. Structural, dielectric and magnetic properties of Gd substituted manganese ferrite nanoparticles. Physica Scripta. 90(8). doi:10.1088/0031-8949/90/8/085809.

Naresh G, Mandal TK. 2014. Excellent Sun-Light-Driven Photocatalytic Activity by Aurivillius Layered Perovskites, $Bi_{5-x}La_xTi_3FeO_{15}$ (x = 1, 2). ACS Appl Mater Interfaces. 6(23):21000–21010. doi:10.1021/am505767c.

Nayak P, Badapanda T, Panigrahi S. 2015. Effect of sintering temperature on electrical properties of SrBi4Ti4O15 ceramics. J Mater Sci: Mater Electron. 26(5):2913–2920. doi:10.1007/s10854-015-2777-x.

Nune KC, Somani MC, Spencer CT, Misra RDK. 2017. Cellular response of *Staphylococcus aureus* to nanostructured metallic biomedical devices: surface binding and mechanism of disruption of colonization. Materials Technology. 32(1):22–31. doi:10.1080/10667857.2015.1112572.

Panchal G, Shukla DK, Choudhary RJ, Reddy VR, Phase DM. 2017. The effect of oxygen stoichiometry at the interface of epitaxial $BaTiO_3$ /$La_{0.7}Sr_{0.3}MnO_3$ bilayers on its electronic and magnetic properties. Journal of Applied Physics. 122(8):085310. doi:10.1063/1.5000133.

Ramos-Corella KJ, Sotelo-Lerma M, Gil-Salido AA, Rubio-Pino JL, Auciello O, Quevedo-López MA. 2019. Controlling crystalline phase of TiO_2 thin films to evaluate its biocompatibility. Materials Technology. 34(8):455–462. doi:10.1080/10667857.2019.1576821.

Rana S, Rawat J, Misra RDK. 2005. Anti-microbial active composite nanoparticles with magnetic core and photocatalytic shell: TiO2–NiFe2O4 biomaterial system. Acta Biomaterialia. 1(6):691–703. doi:10.1016/j.actbio.2005.07.007.

Rana S, Rawat J, Sorensson MM, Misra RDK. 2006. Antimicrobial function of Nd3+-doped anatase titania-coated nickel ferrite composite nanoparticles: A biomaterial system. Acta Biomaterialia. 2(4):421–432. doi:10.1016/j.actbio.2006.03.005.

Rani R, Kumar G, Batoo KM, Singh M. Electric and Dielectric Study of Zinc Substituted Cobalt Nanoferrites Prepared by Solution Combustion Method. American Journal of Nanomaterials.:4.

Rawat J., Rana S, Sorensson MM, Misra RDK. 2007. Anti-microbial activity of doped anatase titania coated nickel ferrite composite nanoparticles. Materials Science and Technology. 23(1):97–102. doi:10.1179/174328407X158488.

Rawat Jagdish, Rana S, Srivastava R, Misra RDK. 2007. Antimicrobial activity of composite nanoparticles consisting of titania photocatalytic shell and nickel ferrite magnetic core. Materials Science and Engineering: C. 27(3):540–545. doi:10.1016/j.msec.2006.05.021.

Sharma S, Singh MM, Rai US, Mandal KD. 2015. Rationalization of dielectric properties of nano-sized iron doped yttrium copper titanate using impedance and modulus studies. Materials Science in Semiconductor Processing. 31:720–727. doi:10.1016/j.mssp.2014.12.069.

Sharma S, Yadav SS, Singh MM, Mandal KD. 2014. Impedance spectroscopic and dielectric properties of nanosized Y 2/3 Cu 3 Ti 4 O 12 ceramic . Journal of Advanced Dielectrics. 04(04):1450030. doi:10.1142/s2010135x14500301.

Shehata MM, Abdelhady K. 2018. Temperature and frequency dependence of dielectric relaxation and AC electrical conductivity in p-Si/CuPc hybrid photodiode. Appl Phys A. 124(9):591. doi:10.1007/s00339-018-2006-6.

Shukla Y, Srivastava, Bhatnagar, Singh, Mishra, Kumar, Gupta. 2013 Apr. Synthesis of PLGA nanoparticles of tea polyphenols and their strong in vivo protective effect against chemically induced DNA damage. IJN.:1451. doi:10.2147/IJN.S26364.

Singh DK, Ganesan V, Yadav DK, Yadav M. 2020. Metal (Mn, Fe, Co, Ni, Cu, and Zn) Phthalocyanine-Immobilized Mesoporous Carbon Nitride Materials as Durable Electrode Modifiers for the Oxygen Reduction Reaction. Langmuir. 36(41):12202–12212. doi:10.1021/acs.langmuir.0c01822.

Singh S, Kumar A, Pandey SK, Kumar V, Verma MK, Gupta A, Mandal KD. 2020 Jun 5. Synthesis of $Bi_4Ti_3O_{12}$-$BaTiO_3$ nanocomposite, manifesting high dielectric and unique magnetic nature applicable in heterogeneous photocatalytic activity for degradation of Rhodamine B dye. Materials Technology.:1–16. doi:10.1080/10667857.2020.1774228.

Sultan K, Ikram M, Gautam S, Lee HK, Chae KH, Asokan K. 2015. Electrical and magnetic properties of the pulsed laser deposited Ca doped LaMnO3 thin films on Si (100) and their electronic structures. RSC Advances. 5(85):69075–69085. doi:10.1039/c5ra08028b.

Sun D, Jin X, Liu H, Zhu J, Zhu Yudan, Zhu Yinyin. 2007. Investigation on FTIR spectrum of barium titanate ceramics doped with alkali ions. Ferroelectrics. 355(1 PART 1):145–148. doi:10.1080/00150190701517630.

Sunkara BK, Misra RDK. 2008. Enhanced antibactericidal function of W4+-doped titania-coated nickel ferrite composite nanoparticles: A biomaterial system. Acta Biomaterialia. 4(2):273–283. doi:10.1016/j.actbio.2007.07.002.

Tellier J, Boullay P, Manier M, Mercurio D. 2004. A comparative study of the Aurivillius phase ferroelectrics CaBi 4Ti4O15 and BaBi4Ti 4O15. Journal of Solid State Chemistry. 177(6):1829–1837. doi:10.1016/j.jssc.2004.01.008.

Thomas AK, Abraham K, Thomas J, Saban K V. 2017. Electrical and dielectric behaviour of Na 0.5 La 0.25 Sm 0.25 Cu 3 Ti 4 O 12 ceramics investigated by impedance and modulus spectroscopy. Journal of Asian Ceramic Societies. 5(1):56–61. doi:10.1016/j.jascer.2017.01.002.

Venkatasubramanian R, Srivastava RS, Misra RDK. 2008. Comparative study of antimicrobial and photocatalytic activity in titania encapsulated composite nanoparticles with different dopants. Materials Science and Technology. 24(5):589–595. doi:10.1179/174328408X282065.

Viezbicke BD, Patel S, Davis BE, Birnie DP. 2015. Evaluation of the Tauc method for optical absorption edge determination: ZnO thin films as a model system: Tauc method for optical absorption edge determination. Phys Status Solidi B. 252(8):1700–1710. doi:10.1002/pssb.201552007.

Wang T, Hu J, Yang H, Jin L, Wei X, Li C, Yan F, Lin Y. 2017. Dielectric relaxation and Maxwell-Wagner interface polarization in Nb2O5 doped 0.65BiFeO3-0.35BaTiO3 ceramics. Journal of Applied Physics. 121(8):0–9. doi:10.1063/1.4977107.

Xiang Q, Yu J, Jaroniec M. 2011. Enhanced photocatalytic H2-production activity of graphene-modified titania nanosheets. Nanoscale. 3(9):3670. doi:10.1039/c1nr10610d.

Yadava SS, Khare A, Gautam P, Kumar A, Mandal KD. 2017. Dielectric, ferroelectric and magnetic study of iron doped hexagonal Ba $_4$ YMn $_3$ O $_{11.5-\delta}$ (BYMO) and its dependence on temperature as well as frequency. New J Chem. 41(11):4611–4617. doi:10.1039/C6NJ04071C.

Zhang L, Wang H, Chen Z, Wong PK, Liu J. 2011 May. Bi2WO6 micro/nano-structures: Synthesis, modifications and visible-light-driven photocatalytic applications. Applied Catalysis B: Environmental.:S0926337311002098. doi:10.1016/j.apcatb.2011.05.008.

Zhang X, Wang X, Wang Q, Ma X, Liu Chunming, Li P, Liu Cailong, Han Y, Ma Y, Gao C. 2018. Hydride ion (H -) transport behavior in barium hydride under high pressure. Physical Chemistry Chemical Physics. 20(13):8917–8923. doi:10.1039/c7cp08386f.

Zhao X, Yang H, Cui Z, Wang X, Yi Z. 2019. Growth Process and CQDs-modified Bi4Ti3O12 Square Plates with Enhanced Photocatalytic Performance. Micromachines. 10(1):66. doi:10.3390/mi10010066.

Zn P, Ti N, Crystal OS. 2017. Switching Characteristics and High-Temperature. :1–10. doi:10.3390/ma10040349.